Received: 26 June 2021 | Revised: 23 November 2021 | Accepted: 14 December 2021

DOI: 10.1002/mrm.29144

RESEARCH ARTICLE

Magnetic Resonance in Medicine

Motion-compensated fat-water imaging for 3D cardiac MRI at ultra-high fields

Sebastian Dietrich[1] | **Christoph Stefan Aigner**[1] | **Johannes Mayer**[1] | **Christoph Kolbitsch**[1] | **Jeanette Schulz-Menger**[2,3,4] | **Tobias Schaeffter**[1,5] | **Sebastian Schmitter**[1,6]

[1]Physikalisch-Technische Bundesanstalt (PTB), Braunschweig and Berlin, Germany

[2]Experimental and Clinical Research Center, A Joint Cooperation between the Charité Medical Faculty and the Max-Delbrueck Center for Molecular Medicine and HELIOS Hospital Berlin Buch, Berlin, Germany

[3]DZHK (German Center for Cardiovascular Research), Partner Site Berlin, Berlin, Germany

[4]Helios Clinics Berlin-Buch Department of Cardiology and Nephrology, Berlin, Germany

[5]Department of Medical Engineering, Technische Universität Berlin, Germany

[6]Center for Magnetic Resonance Research, University of Minnesota, Minneapolis, Minnesota, USA

Correspondence
Sebastian Dietrich, Physikalisch-Technische Bundesanstalt (PTB), Brauschweig and Berlin, Abbestraße 2-12, 10587 Berlin, Germany.
Email: sebastian.dietrich@ptb.de

Funding information
German Research Foundation, Grant/Award Number: GRK2260-BIOQIC and SCHM 2677/2-1

Purpose: Respiratory motion-compensated (MC) 3D cardiac fat-water imaging at 7T.

Methods: Free-breathing bipolar 3D triple-echo gradient-recalled-echo (GRE) data with radial phase-encoding (RPE) trajectory were acquired in 11 healthy volunteers (7M\4F, 21–35 years, mean: 30 years) with a wide range of body mass index (BMI; 19.9–34.0 kg/m^2) and volunteer tailored B_1^+ shimming. The bipolar-corrected triple-echo GRE-RPE data were binned into different respiratory phases (self-navigation) and were used for the estimation of non-rigid motion vector fields (MF) and respiratory resolved (RR) maps of the main magnetic field deviations (ΔB_0). RR ΔB_0 maps and MC ΔB_0 maps were compared to a reference respiratory phase to assess respiration-induced changes. Subsequently, cardiac binned fat-water images were obtained using a model-based, respiratory motion-corrected image reconstruction.

Results: The 3D cardiac fat-water imaging at 7T was successfully demonstrated. Local respiration-induced frequency shifts in MC ΔB_0 maps are small compared to the chemical shifts used in the multi-peak model. Compared to the reference exhale ΔB_0 map these changes are in the order of 10 Hz on average. Cardiac binned MC fat-water reconstruction reduced respiration induced blurring in the fat-water images, and flow artifacts are reduced in the end-diastolic fat-water separated images.

Parts of this work have been presented at the 2021 virtual annual meeting of the International Society for Magnetic Resonance in Medicine.

This is an open access article under the terms of the Creative Commons Attribution License, which permits use, distribution and reproduction in any medium, provided the original work is properly cited.
© 2022 Physikalisch-Technische Bundesanstalt. *Magnetic Resonance in Medicine* published by Wiley Periodicals LLC on behalf of International Society for Magnetic Resonance in Medicine.

Conclusion: This work demonstrates the feasibility of 3D fat-water imaging at UHF for the entire human heart despite spatial and temporal B_1^+ and B_0 variations, as well as respiratory and cardiac motion.

KEYWORDS

7 Tesla, B_0, body imaging, Dixon, fat-water imaging, parallel transmission, respiration

1 | INTRODUCTION

Fat-water (FW) cardiac MR (CMR) imaging is an essential technique for assessing fatty infiltration of the myocardium.[1] Especially the differentiation of epicardial fat from intramyocardial fat remains difficult for the right ventricle with its thin structure, and overall small, affected areas in the myocardium compared to the limited resolution of current systems, and currently fail for the assessment of disease like arrhythmogenic right ventricular cardiomyopathy.[2,3] Therefore, a histologic evaluation of the biopsied right ventricular endomyocardial tissue is still part of the recommendation.[4]

To determine the FW content in the human body, chemical shift encoding-based techniques have become an established clinical imaging method.[5–7] These techniques use different TEs to encode the FW information into the magnitude and phase of the MR signal. To resolve ambiguity problems, particularly in the presence of main magnetic field deviations (ΔB_0), triple gradient-recalled echo (GRE) methods[8,9] were proposed. The latter enables direct estimation of the ΔB_0 inhomogeneities, which can be used to resolve the ambiguity problem.[10–12] Thereby, the separation of the images into fat and water content can be performed sequentially[13,14] or in a joint reconstruction.[15,16] To date, 3D multi-echo GRE FW imaging techniques have been applied to the entire human body[10] as well as to various organs[8,17,18] at field strengths up to 3T.

However, by increasing the field strength, toward ultra-high fields (UHF >= 7T), especially 3D FW imaging may benefit due to an increased SNR and spectral separation. Moreover, another benefit may be the reduction of the relative influence of j-coupling, which could improve the quantification of saturated and unsaturated fatty acids, as recently shown for lower fields.[19,20] In previous 7T body studies, the water or fat signal at UHF has been obtained by using 3D fat or water selective rectangular pulses for pelvic lymph node detection,[21] or by suppressing the fat signal with spectral pulses in 3D coronary angiography.[22] While, successful water and fat imaging has been demonstrated in breast imaging at 7T using a dual-echo GRE acquisition,[23] to the best of the author's knowledge, no investigations have been performed for UHF cardiac MRI using a multi-echo, cardiac binned (CB), and respiration resolved (RR) acquisition.

This gap may be linked to the fact that 3D imaging at UHF in the human body and, in particular, the heart is highly challenging due to multiple factors. First, the increased transmit field (B_1^+) heterogeneity in the body at UHFs, leads to an inhomogeneous flip angle (FA) distribution, including regions of complete signal cancelation within the volume of interest.[24,25] This issue has been addressed by volunteer-tailored parallel transmission techniques (pTx), such as B_1^+ phase shimming,[26–28] spokes,[29,30] kT-point[24] and, recently, using calibration-free universal pulses.[31] Another technique that does not require volunteer-specific B_1^+ information but provides homogeneous image without signal dropouts is the time-interleaved acquisition of modes (TIAMO) technique.[21,32]

Second, cardiovascular MRI (CMR), and particularly 3D CMR, is generally more challenging compared with brain MR applications because of the cardiac and respiratory motion that can decrease image quality.[33,34] Different strategies to handle cardiac motion were proposed[35,36], however, most strategies rely on the acquisition of an electrocardiogram (ECG), and it has been shown that the ECG signal is strongly affected by the magnetohydrodynamic effect at 7T yielding incorrect ECG trigger points.[37] This has been especially a problem in long 3D hemodynamic scans performed under free-breathing at 7T that had to be aborted after some time and restarted with a different ECG detection algorithm.[25] The 3D FW imaging scans also require scan times of approximately 8–12 minutes[17,38]; thus, similar issues could arise in FW scans performed at UHF. To mitigate respiratory-induced artifacts, breath-holds can be used in 2D acquisitions, but scan durations of 3D acquisitions covering the body are typically longer than a breath-hold. Thus, 3D acquisitions are usually obtained under free-breathing in combination with image-based navigators, which track the motion of the liver. However, while this method is effective at lower field strengths, it may fail at UHF, since the navigator performance strongly depends on the B_1^+ shim setting.[25] One efficient way to overcome this problem consists in using free-breathing acquisitions in combination with self-navigation approaches[39,40] that bin or gate the acquired k-space data into different motion phases reflecting the respiratory position.[41] Additionally, self-navigation can

be combined with respiratory motion correction[42–45] to increase the scan efficiency and use up to 100% of the acquired data.

Another challenge of FW imaging that is even observed at 1.5T or 3T is given by ΔB_0 variations across the target region. At UHFs, however, ΔB_0, as well as its spatial and temporal variations are larger compared with lower field strengths.[46,47] In addition, potential fluctuations in ΔB_0 as a function of the respiratory phase have been demonstrated at UHFs for the human heart,[48] showing local ΔB_0 changes of up to 100 Hz between exhale and deep inhale. These respiration-induced ΔB_0 changes may have an impact on free-breathing 3D FW imaging at UHFs, especially when different respiratory phases are combined. This is because a respiratory-dependent B_0 would result in different ΔB_0 information from different respiratory phases[16] being combined in one image due to non-respiratory motion resolved reconstruction or motion compensation, which could lead to FW swaps in the resulting separated images.

In the present work, we investigate the feasibility of obtaining free-breathing 3D triple-echo GRE data for respiratory motion-compensated (MC) and CB FW imaging at 7T. After volunteer-tailored homogenous B_1^+ shimming across the whole heart the triple-echo GRE data are binned into different respiratory phases, separate datasets for each respiratory phase are reconstructed and 3D respiratory motion vector fields (MF) are estimated using a non-rigid registration approach.[49] Since the MC step assumes static ΔB_0 for each moving voxel, respiratory phase-resolved ΔB_0 maps are calculated to investigate the resulting ΔB_0 changes throughout the respiratory cycle, and motion-corrected ΔB_0 fields are calculated. Finally, a joint reconstruction based on the triple-echo GRE dataset using the electrocardiogram (ECG) information, the calculated MF, a motion-corrected ΔB_0 estimate, and a six-peak signal model for fat is applied to reconstruct respiratory MC and CB 3D FW images of the heart at UHF.

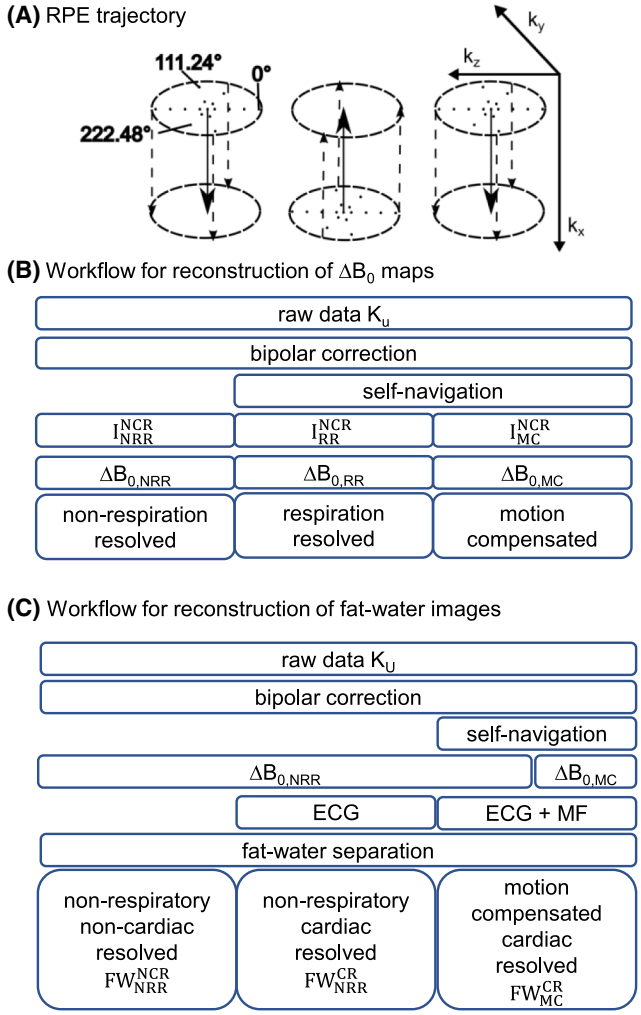

FIGURE 1 Overview of the trajectory and workflow used to obtain main magnetic field inhomogeneity (ΔB_0) maps and FW images. A, Schematic depiction of bipolar RPE trajectory with arrows indicating readout direction, with golden angle increment of 111.24° between successive spokes. B, Block diagram of the reconstruction workflow to obtain ΔB_0 maps of different motion phases, that is, NRR, RR, and respiratory MC. C, Block diagram of reconstruction workflow to obtain FW images in different RR, NCB, and CB motion phases, detailed in the motion handling subsection

2 | METHODS

The 3D triple-echo GRE data, based on a radial phase-encoding (RPE) trajectory[39] (cf. Figure 1A), were acquired (cf. Table 1), reconstructed, and separated into fat and water images. For reconstruction, an iterative, model-based reconstruction framework[15] was used that utilizes parallel imaging,[50] compressed sensing,[51] motion information,[52] and a multi-peak spectral model for fat to account for chemical shift effects. The various steps required to obtain 3D FW separated images and RR ΔB_0 maps of the heart at UHF are presented below.

2.1 | Experimental setup

All MRI scans were performed on a 7T system (Magnetom 7T, Siemens Healthineers, Germany) equipped with an eight-channel pTx system. Imaging was performed with a commercial thorax coil array (MRI Tools, Berlin, Germany) consisting of 32 transceiver elements (eight dipoles and 24 loops) operated in an 8Tx\32Rx channel mode. The detailed setup of the coil, as well as the applied power limits, were identical to previous publications.[24,41] The study was performed after obtaining ethical approval by the local institutional review board and after

TABLE 1 Sequence parameter including TR, TE, TA, FA, FOV, readout BW, and self-navigation TS

	Relative 3D B_1^+	3D AFI	Triple-echo GRE-RPE
TR1 [TR2] (ms)	5	10 [50]	6.1
TE (ms)	2.02	2.02	1.51/2.79/4.07
TA (min)	3.40	6.00	9.17
Reduction factor R	2.50	2.20	0.84
Nominal FA (°)	20	90	25
Actual FA (°)			5 ± 1
Reference voltage (V)	170		
FOV (mm^3)	$250 \times 312–350 \times 312–350$		
Voxelsize (mm^3)	$4 \times 4 \times 4$	$4 \times 4 \times 4$	$1.4 \times 1.4 \times 1.4$
BW (kHz)	25.54	25.54	227.22
TS (ms)	80	480	268
Spokes	256	384	2048
PE per spoke	16	12	44

Note: The reduction factor R is given by the ratio of the number of phase encoding (PE) points requiered for a fully sampled RPE scan to the number of acquired PE points.

providing written informed consent from 11 healthy volunteers (age: 30 ± 5 years; max\min: 35\21 years; body mass index: 24 ± 5 kg/m^2; max\min: 34\19 kg/m^2; male\female: 7\4). A three-lead wireless ECG was used for retrospective cardiac phase binning, following Ref. [37]. Leads were placed by the operators with volunteers lying in a supine, head-first position on the table prior to coil placement. After placing the coil centrally over the heart and positioning the table into the isocenter, ECG triggering performance was evaluated at the host console. It was visually checked whether (i) other peaks were falsely detected in addition to the R-peak, (ii) the detection of the R-wave correlated with the signal from the infrared plethysmograph attached to the left index finger, and (iii) there was any potential jitter in the R-peak detected by the scanner. If the trigger performance was insufficient, the trigger mode was first changed, and if this was not sufficient, the electrodes were replaced and the procedure was repeated. The default (tune-up) B_0 shim was applied and the center frequency was set to the water peak using the semiautomatic adjustment routine of the system.

2.2 | B_1^+ calibration

All volunteers underwent the same protocol. In addition, a high-resolution 3D triple-echo GRE-RPE scan was performed for the last volunteer, further described below. Each protocol started with the default B_1^+ shim setting ϕ_0 of the coil, set by the manufacturer and optimized based on electromagnetic simulations for the ascending and descending aorta. This default phase setting, however, may result in signal cancellations in some volunteers. Therefore, relative 3D B_1^+ mapping was performed using a 3.40 minutes long free-breathing 3D GRE-RPE acquisition as outlined in Ref. [41]. Scan parameters are listed in Table 1. Since only a *shallow*-breathing pattern was requested, strong respiration-induced variations of B_1^+ were not expected; therefore, motion-averaged relative 3D B_1^+ datasets were extracted.[41] The raw data were transferred to a separate workstation (RAM: 128 GB; CPUs: 12 with 2.1 GHz) and B_1^+ maps were reconstructed using MATLAB R2019b (MathWorks, Natick, MA, USA) with 4 mm isotropic resolution within approximately 1 minute. Either B_1^+ phase or B_1^+ magnitude and phase shimming was subsequently performed on three transversal slices across the heart, as indicated in Figure 2, to obtain a homogenous B_1^+ distribution within the heart, similar to Ref. [41]. Actual FA imaging (AFI) was performed[53] during RF shim calculation to quantify the average FA within the target region. This analysis, however, was only performed retrospectively due to the tight timing of the protocol.

2.3 | 3D triple-echo GRE-RPE imaging protocol

After applying the calculated B_1^+ shim, 3D triple-echo GRE-RPE data with 1.4 mm^3 isotropic resolution and an actual FA of 5° were acquired in 9.17 minutes (spokes: 2048; phase-encoding points per spoke: 44; reduction factor (R): 0.84, bandwidth (BW): 227.22 kHz, self-navigation sampling time (TS): 268 ms). Further parameters are listed in Table 1. For the last volunteer (V11) the same protocol was acquired, except that one additional 3D

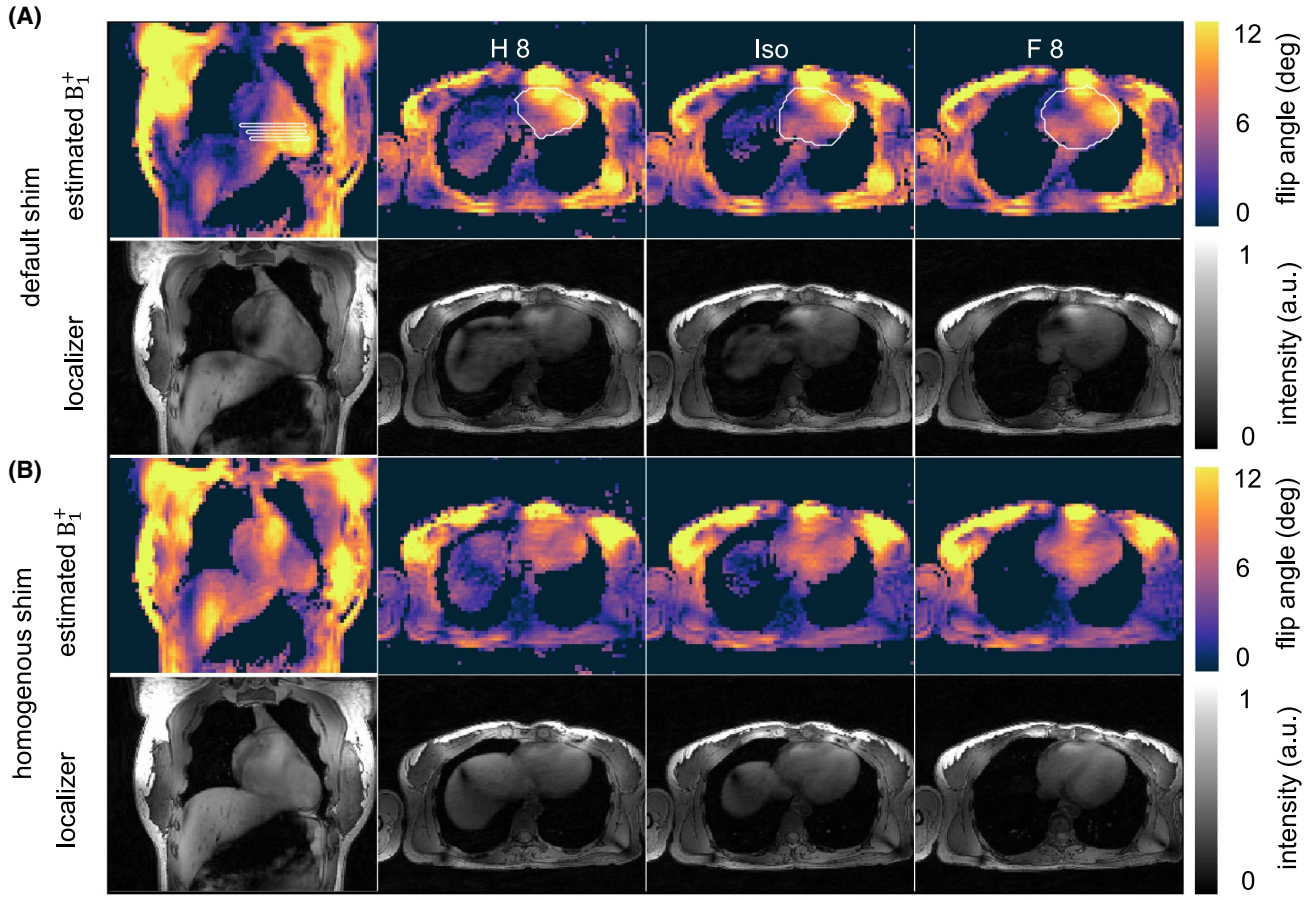

FIGURE 2 Estimated absolute B_1^+ distribution in one coronal and three transversal slices, for a slice 8 mm above (H 8) and below (F 8) the isocenter (iso). Corresponding localizer images for matching coronal and transversal slices obtained with default (A) and volunteer tailored (B) B_1^+ shim. Images are taken from volunteer V9

triple-echo GRE-RPE dataset with 1.1 mm^3 isotropic resolution was obtained within 11.7 minutes (spokes: 1920; phase-encoding points per spoke: 60; R: 1.06; BW: 294.11 kHz; TS: 366 ms) with remaining parameters kept identically to the 1.4 mm^3 scans. For post-processing, 3D triple echo GRE data were transferred to a separate workstation (1 TB RAM, 24 CPUs at 3.0 GHz) and reconstructed using MATLAB R2019b (MathWorks, Natick, MA, USA).

2.4 | Bipolar gradient correction

Prior to the reconstruction of the FW images and the calculation of the estimated ΔB_0 maps, phase errors resulting from the bipolar readout gradient polarity were corrected.[54] Therefore, the bipolar-uncorrected 3D triple-echo GRE-RPE k-space data (K_u) were reconstructed into non-RR (NRR) and non-CB (NCB) images using an iterative SENSE algorithm.[50] Constant and linear phase terms of the second echo with respect to the first and third echo were estimated in the image domain along the readout direction for each volunteer. Then the second echo $K_u(TE_2)$ is corrected for the constant and linear phase terms to obtain bipolar corrected triple-echo GRE-RPE data (K).

2.5 | Motion handling

Respiratory MC was applied to transform data from different respiratory phases into a single respiratory reference phase, which was set as the end-exhale phase. MC increases the sampling density in the resulting k-space dataset compared with the respiratory binned k-space datasets and, thus, reduces undersampling as well as motion artifacts in the resulting reconstructed MC images I_{MC}. A particular aspect to consider in MC is the potential fluctuation of ΔB_0 during respiration, which could lead to erroneous MC, NCB ΔB_0 maps ($\Delta B_{0,MC}$) derived from I_{MC} and, thus, may result in erroneous FW images. To investigate this aspect, we first separated the data into different respiratory phases to analyze the impact of respiration as well as MC on the resulting ΔB_0 maps (cf. Figure 1B).

To examine the impact of respiratory motion and MC, the triple-echo GRE-RPE dataset K was binned into

different respiratory phases using self-navigation using a sliding window with 30% overlap to the next respiratory bin. Then, the datasets were reconstructed into four RR and NCB triple-echo images $I_{RR}^{NCB} = \{I_{exhale}, ..., I_{inhale}\}$ using iterative SENSE. For self-navigation, a motion surrogate was estimated from the central k-space line of each RPE spoke from the first echo K(TE1).[40] Subsequently, a non-rigid MF was determined for each respiratory phase from the RR images of the first echo $I_{RR}^{NCB}(TE_1)$ using NIFTYREG.[49] Therein, the MFs describe the pixel's displacements from a respiratory phase to the reference phase. These MFs were used for MC image reconstruction[42] of K to obtain MC and NCB images I_{MC}^{NCB} that were used for the calculation of $\Delta B_{0,MC}$.

In addition, NRR and NCB, NRR and CB, and MC and CB FW images FW_{NRR}^{NCB}, FW_{NRR}^{CB}, and FW_{MC}^{CB} were derived from the same datasets K (cf., Figure 1C), with FW_{MC}^{CB} being reconstructed with $\Delta B_{0,MC}$, and NRR, NCB ΔB_0 maps ($\Delta B_{0,NRR}$). Therefore, the bipolar-corrected dataset K was retrospectively split into five different cardiac phases using the recorded ECG signal with a sliding window and a 30% overlap to the next cardiac bin to obtain FW_{NRR}^{CB} images with compressed sensing[15] reconstruction techniques. The acquisition window of each phase depends on the heart rate and corresponds to ~200 ms per cardiac phase. For the reconstruction of MC and CB images, the bipolar-corrected dataset K was first divided into the five cardiac phases and each cardiac phase dataset was divided into the different respiratory motion phases to apply the MF during compressed sensing reconstruction of FW_{MC}^{CB}.

2.6 | Estimation of ΔB_0

To investigate changes of ΔB_0 as a function of the respiratory cycle images I_{NRR}^{NCB}, I_{RR}^{NCB} and I_{MC}^{NCB} (cf. Figure 1B) were used to calculate the corresponding ΔB_0 maps with a multi-seeded safest-first region-growing algorithm outlined in Ref. [10]. It uses an analytic function to find ΔB_0 values for each voxel, identifies true seed voxels over the entire volume, and grows a ΔB_0 map.

2.7 | Reconstruction of fat and water images

Three different types of FW images were reconstructed: (1) FW_{NRR}^{NCB}, (2) FW_{NRR}^{CB}, and (3) FW_{MC}^{CB}. $\Delta B_{0,NRR}$ were used to reconstruct (1), (2), and (3), whereas $\Delta B_{0,MC}$ were also used to reconstruct (3), as shown in Figure 1C. To obtain the fat and water images, a signal-model-based compressed sensing reconstruction was performed afterward.[15,38] The acquired multi-echo data are assumed to be composed of the water signal W, precessing at a single frequency, and the fat signal F, which is modeled by a six-peak spectrum as used by the "FattyRiot" toolbox,[55] with fixed frequency shifts [−1129 Hz, −1010 Hz, −772 Hz, −576 Hz, −115 Hz, 178 Hz] and relative amplitude of the spectral peaks [0.087, 0.693, 0.128, 0.004, 0.039, 0.048]. A compressed sensing reconstruction was performed on bipolar-corrected raw data K by solving the following minimization problem:

$$\operatorname{argmin}\left(\|\mathrm{E}(\mathrm{W},\mathrm{F})-\mathrm{K}\|_2^2+\lambda_{FW}\|\mathrm{TV}(\mathrm{W},\mathrm{F})\|_1+\lambda_t\|\mathrm{TVT}(\mathrm{W},\mathrm{F})\|_1\right), \quad (1)$$

with spatial total variation term TV for each motion phase and the total variation term TVT along the motion phases. λ_{FW} and λ_t are the spatial and temporal regularization parameters used to set the tradeoff between data consistency $\|E(W,F)-K\|_2^2$ and minimization of undersampling artifacts. E is the forward operator, transforming the water images W and fat images F to k-space, and it contains the gridding operator, the FFT, the six-peak fat model, coil sensitivity maps,[56] MFs, and the ΔB_0 maps. The regularization parameters were optimized on the first volunteer and then retained for all volunteers. λ_t is set to zero for non-resolved motion phase reconstruction, and the MFs are only used for MC reconstruction. Reconstruction of FW images with 1.4 mm^3 isotropic resolution took 4 h for FW_{NRR}^{NCB} and up to 10 h for FW_{MC}^{CB} images.

2.8 | Data analysis

For the retrospective assessment of the actual FA, channel-wise relative B_1^+ maps were calibrated with an absolute AFI map as outlined in Ref. [41] to obtain estimated, absolute B_1^+ maps. This retrospective evaluation was performed after the measurement due to tight scan time restrictions. Using the absolute B_1^+ maps, the mean and the SD of the actual FA for the entire heart (ROI_{B1}) were determined. The determined ROI_{B1} was manually defined for each transversal slice along the heart-lung boundary, with the coefficient of variation (CV) defined as in Ref. [41].

ΔB_0 maps were then analyzed within a 3D ROI (ROI_{B0}) covering the entire heart for each volunteer and each respiratory phase. Therefore, manually defined 2D ROIs covering the heart in six transversal slices for every respiratory phase were created with a 10 – 18 mm spacing between slices in the head-foot (HF) direction. ROI_{B0} with full heart coverages was then generated by interpolating the 2D ROIs in HF direction between the slices in MATLAB R2019b (function: INTERPMASK, MathWorks, Natick, MA, USA). ΔB_0 maps are given in Hz and subsequently, the SD of each ΔB_0 distribution within ROI_{B0} was determined. To compare two masked ΔB_0 maps in different respiratory phases, the center frequency difference Δf_0

and the SD of the voxel-wise difference between the two ΔB_0 maps was determined.

The ECG trigger efficiency was retrospectively assessed for all subjects and the entire triple-echo GRE-RPE data acquisition. This was performed by visual comparison of the locations of the detected trigger points by the scanner's trigger routine and the locations of the R-peaks in the ECG curve that are identified by the operator. The trigger efficiency was then defined as the ratio of R-peaks aligned with the detected trigger points to the total number of identified R-peaks in the ECG signal.

Fat-fraction (FF) images were calculated from W and F magnitude images as follows[57]:

$$FF = |F| / (|W| + |F|).$$

3 | RESULTS

Figure 2 shows the estimated absolute B_1^+ map and corresponding GRE-RPE image for volunteer V9 (BMI: 22.3 kg/m^2) with default and homogenous B_1^+ shim after optimization. Qualitatively, the estimated B_1^+ maps match the magnitude of the localizer images and predict the resulting signal intensities. Note, that receive profiles were not corrected. Quantitatively, the CV (mean ± SD) across the entire heart (ROI_{heart}) and all volunteers was reduced from 42 ± 4% for ϕ_0, to 24 ± 4% for homogenous B_1^+ shim while the average FA for all volunteers remained unchanged (5 ± 2° for ϕ_0, 5 ± 1° for homogenous B_1^+ shim).

The impact of respiration on the resulting ΔB_0 maps in one representative volunteer V2 (BMI: 21.0 kg/m^2) is shown in Figure 3. Note, that the tune-up B_0 shim setting

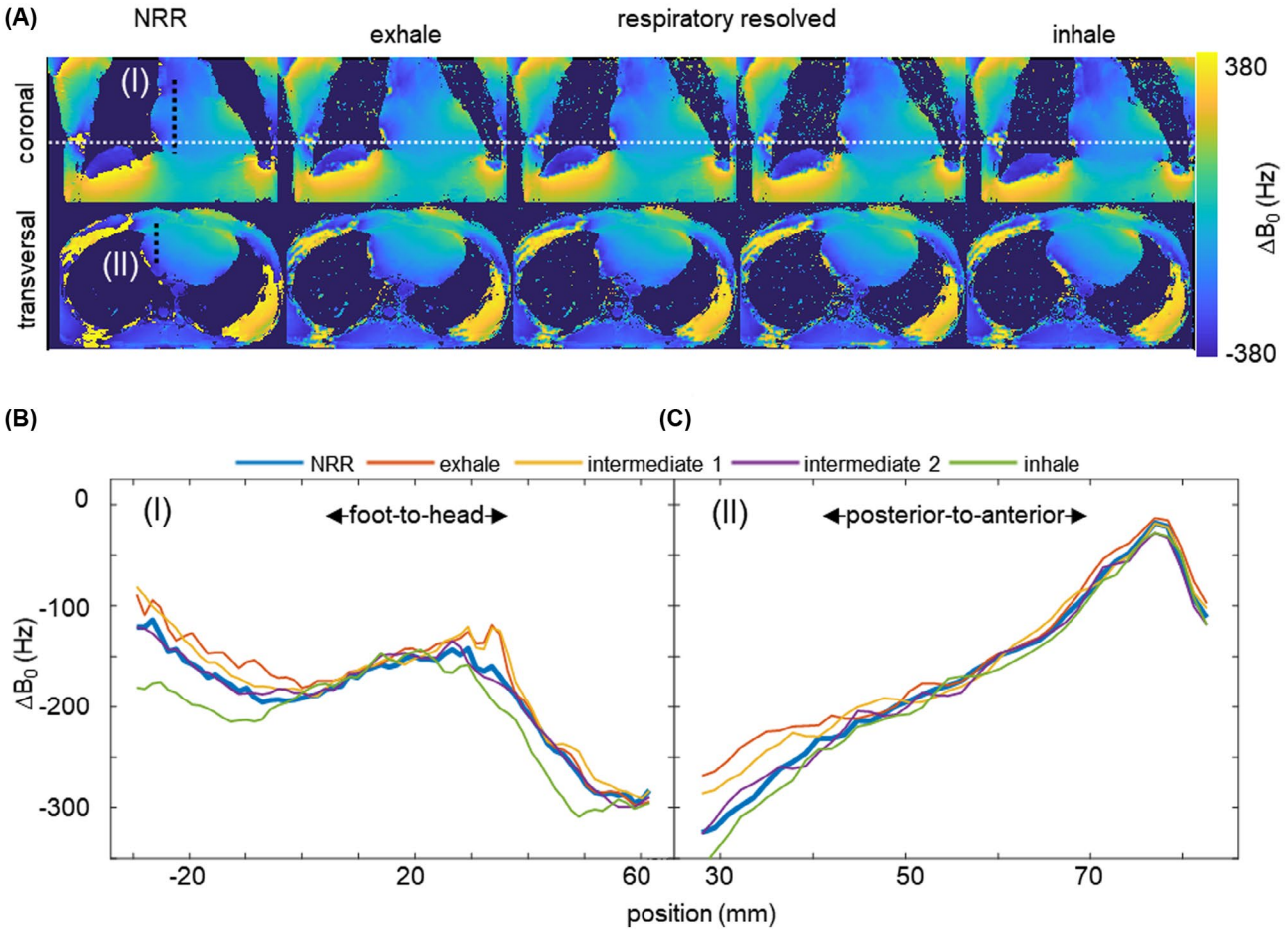

FIGURE 3 A, Coronal and transversal view of ΔB_0 distributions for NRR and RR $\Delta B_{0,RR}$ maps from exhale to inhale motion state. Note $\Delta B_{0,RR}$ are filtered. The dotted white line serves as a guide for the eye to illustrate the movement of the liver through the respiratory phases. Mean (±SD) displacement of 9.8 ± 1.4 mm of right hemidiaphragm position between exhale and inhale was determined. NRR ΔB_0 range across the heart amounts to 450 Hz for the coronal slice and 400 Hz for the transversal slice. B,C, Line plots for foot-to-head (I) and posterior-to-anterior (II) direction are indicated in (A) as black dotted lines. In the foot-to-head direction, a maximum difference between inhale and exhale motion state of −90 Hz, for NRR and exhale of −70 Hz, a mean Δf_0 (±SD) between exhale and inhale of 29 ± 25 Hz, and between NRR and exhale\inhale of −13 ± 12\19 ± 19 Hz in is calculated. In posterior-to-anterior direction (II) a maximum difference between inhale and exhale motion state of −91 Hz, for NRR and inhale of 50 Hz, a mean Δf_0 (±SD) between exhale and inhale of 26 ± 24 Hz, and between NRR and exhale\inhale of −16 ± 18\9 ± 8 Hz is calculated. Images were taken from volunteer V2

was used throughout this work. Filtered RR ΔB_0 maps ($\Delta B_{0,RR}$) maps for four different respiratory phases are shown in Figure 3A in coronal and transversal orientations. Qualitatively, no undersampling or motion artifacts were observed in the different respiratory phases, yielding high-quality ΔB_0 maps that reflect only subtle changes of $\Delta B_{0,RR}$ over the different respiratory phases. Furthermore, similar maps were obtained for the NRR ΔB_0 maps ($\Delta B_{0,NRR}$) compared with $\Delta B_{0,RR}$ with the largest differences of 70 Hz between the inhale and the NRR phase, which is particularly reflected in the line plots (Figure 3B) along the dotted lines indicated in Figure 3A. For $\Delta B_{0,NRR}$, the ΔB_0 range across the heart was 450 Hz for the coronal slice and 400 Hz for the transversal slice (cf., Supporting Information Figure S1, which is available online, for non-filtered $\Delta B_{0,RR}$ maps).

Similar results were found across all volunteers, as shown in Figure 4, where ΔB_0 histograms for the entire 3D ROI_{B0} are illustrated for each volunteer with Δf_0 and SD values for exhale and inhale (cf., Supporting Information Figure S2 showing ROI_{heart} in exhale motion phase). While the shape of the distributions barely changes between exhale and inhale, each distribution appears to be shifted between inhale and exhale. Quantitatively, most of the ΔB_0 values, that is, 95%, are within a range of 460 ± 50 Hz for the whole heart. The SD averaged across all volunteers is 117 Hz\122 Hz for ex-\inhale phase with a mean center frequency shift Δf_0 between inhale and exhale of −15 Hz.

Figure 5 illustrates voxel-wise differences of $\Delta B_{0,RR}$ after applying the MFs, transforming each respiratory phase to the exhale phase, and subtracting the exhale $\Delta B_{0,RR}$ map. Maximum differences are seen for the motion-corrected

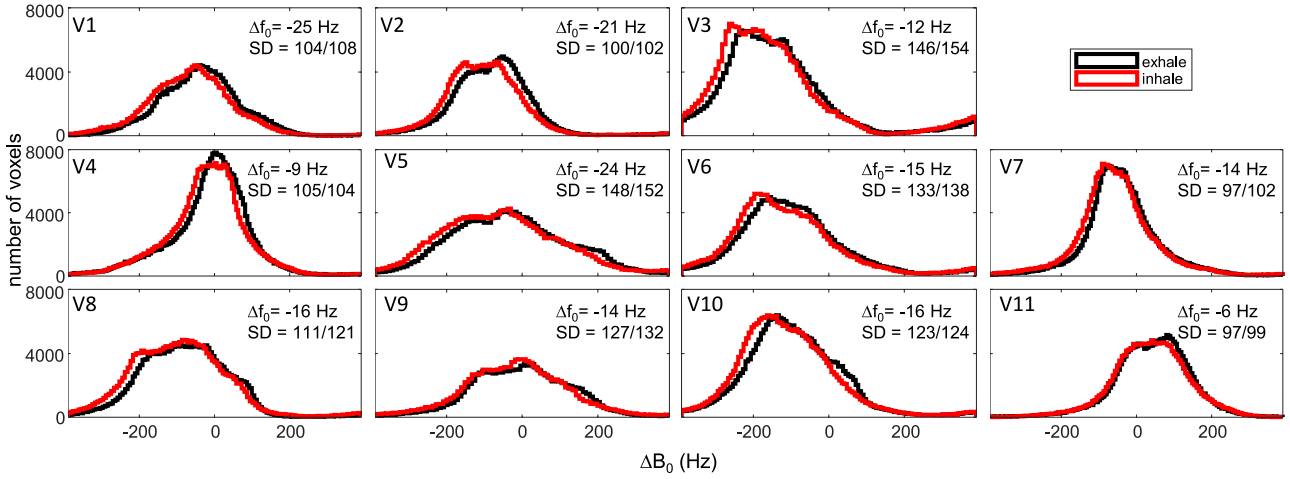

FIGURE 4 Pixelwise main magnetic field deviation (ΔB_0) values are displayed in histograms, whereby the data are taken from different ROI_{heart} for every respiratory phase and all 11 volunteers (cf. Supporting Information Figure S2 for ROI_{heart} in exhale motion phase for each volunteer). With center frequency shift Δf_0 between exhale and inhale, and SD of exhale and inhale motion phase given in right corner of each histogram. Mean Δf_0 of −15 Hz between inhale and exhale, and mean SD of 120 Hz (min\max: 97\150 Hz) for inhale and exhale motion state across all volunteers are calculated

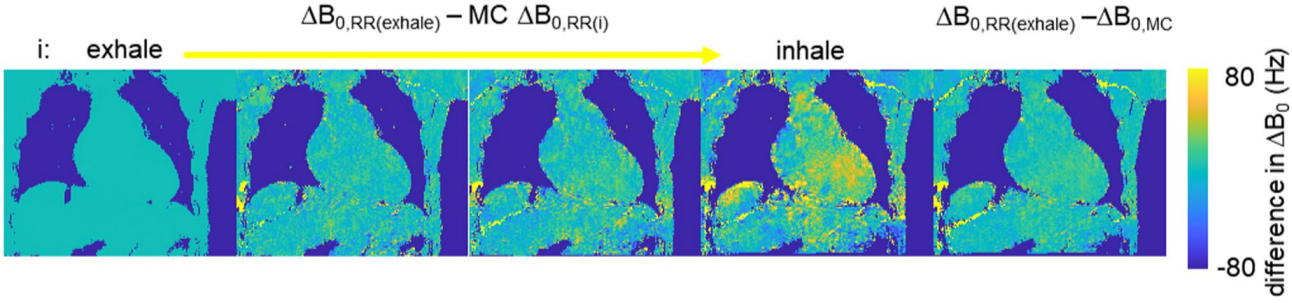

FIGURE 5 ΔB_0 differences maps of different RR and MC phases are shown for coronal slices of volunteer V7. The first four images show the difference between the ΔB_0 map in the exhale phase ($\Delta B_{0,RR(exhale)}$) and the four RR and subsequently MC ΔB_0 maps (MC $\Delta B_{0,RR(i)}$) from exhale to inhale phase. The mean center frequency shift (Δf_0) between $\Delta B_{0,RR(exhale)}$ and MC inhale $\Delta B_{0,RR}$ map with −14 Hz and a mean SD of 35 Hz is calculated. The last image shows the difference between $\Delta B_{0,RR(exhale)}$, and $\Delta B_{0,MC}$ with a mean Δf_0 of −4 Hz, and a mean SD of 16 Hz

inhale maps (fourth column) with maximum and mean Δf_0 ($\pm$SD) of -90 and -14 ± 35 Hz across the whole heart for volunteer V7 (BMI: 20.0 kg/m^2). The last column shows differences in ΔB_0 between the $\Delta B_{0,MC}$ map taking all respiratory phases into account and the exhale $\Delta B_{0,RR}$ map. Here, only marginal differences are observed with a maximum and mean Δf_0 ($\pm$SD) of -40 and -4 ± 16 Hz. Similar values were found for the other volunteers. Overall, these findings demonstrate that the local respiration-induced frequency shift in the order of 10 Hz on average is small compared with the chemical shifts used in the multi-peak model in which more than 90% of the signal has a >700 Hz frequency shift with respect to the water peak. The resulting frequency shift in the $\Delta B_{0,MC}$ map compared to the exhale $\Delta B_{0,RR}$ map amounts to less than 2% of this value, as well as roughly 10% to the fat peak at -115 Hz, which accounts for 4% of the fat signal.

Figure 6 shows the resulting FW images of V2 in a coronal slice for FW^{NCB}_{NRR} images using 100% of the acquired data, for FW^{CB}_{NRR} images in the diastolic phase using only 30% of the data throughout the cardiac cycle, and for FW^{CB}_{MC} images in the diastolic phase (also 30% of the data) with $\Delta B_{0,\ NRR,}$ and $\Delta B_{0,MC}$ maps. Qualitatively, cardiac binning decreases the fat signal in F^{CB}_{NRR} and F^{CB}_{MC} compared with F^{NCB}_{NRR} in the blood pool (Figure 6, blue arrows), due to the reduced impact of blood flow that alters the signal phase especially during systole, likely due to a first gradient moment induced phase accumulation of moving spins in the systolic phase (cf., Supporting Information Video S1). This flow-induced effect is as well visible in the line plot shown in Figure 6B denoted by the blue arrow. Due to the reduced flow in the diastolic phase of FW^{CB}_{MC} and FW^{CB}_{NRR}, this artifact is reduced by approximately 50% compared with FW^{NCB}_{NRR}. Motion blurring is reduced due to the applied MF in FW^{CB}_{MC} compared with the NRR images as denoted by the yellow arrows in Figure 6. This is also reflected in the increased fat signal in FW^{CB}_{MC} (cf., Figure 6 B, red arrow) for both $\Delta B_{0,NRR,}$ and $\Delta B_{0,MC}$ reconstruction. Here, the compensation of the underlying respiratory motion leads to a 60% and 90% higher signal and a reduction of the FWHM of 11% and 27% compared with F^{CB}_{NRR}. The resulting FW images of the remaining volunteers are shown in Supporting Information Figure S3.

The trigger efficiency was retrospectively investigated and showed a mean value of 99.7% across 10 out of 11 volunteers. Figure 7A shows an exemplary ECG signal curve of channel I obtained from volunteer V7 for 90 s and 25 s. As can be seen, the R-peak is detected correctly by the scanner in all but one case; for the entire acquisition, 4 of 438 were not correctly detected, resulting in a trigger efficiency of 99.1%. In one volunteer (V6), the efficiency

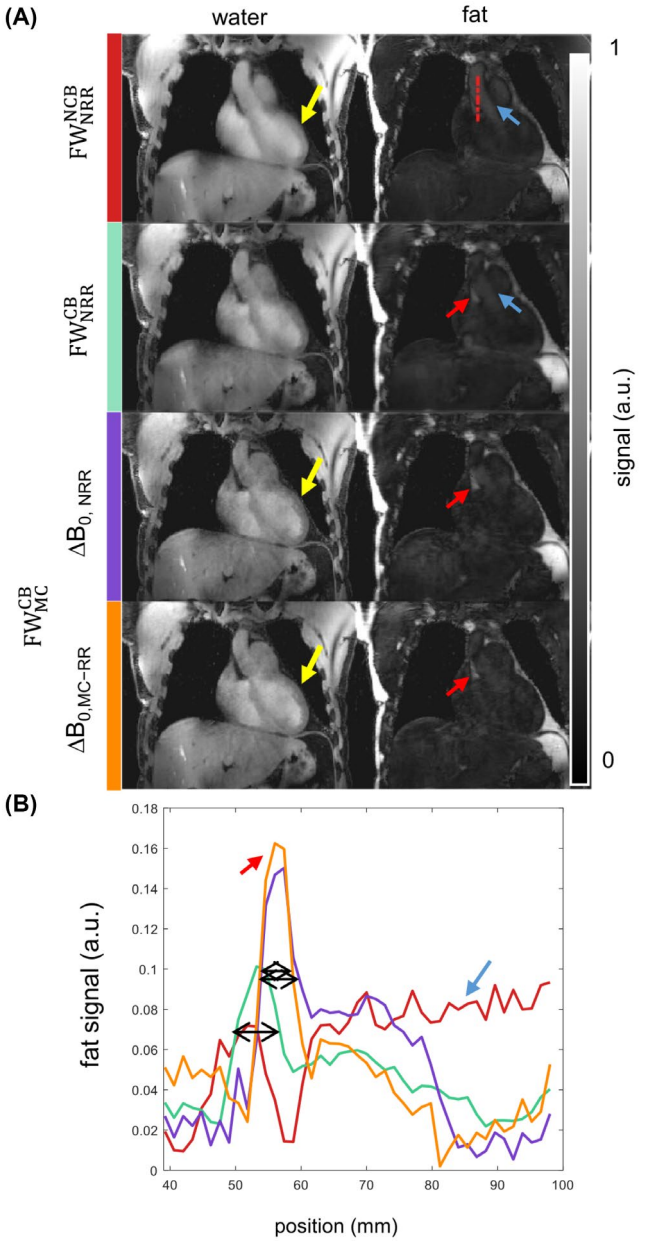

FIGURE 6 A, Resulting in vivo FW images of V2 in a coronal slice are shown for NRR and NCB FW image (FW^{NCB}_{NRR}), NRR and CB FW image (FW^{CB}_{NRR}), and respiratory MC and CB FW image (FW^{CB}_{MC}) reconstruction, with $\Delta B_{0,NRR,}$ and $\Delta B_{0,MC}$ maps used for reconstruction. The CB images are shown in the end-diastolic phase. Improved image quality in MC and CB FW images compared to FW^{NCB}_{NRR}, and FW^{CB}_{NRR} are visible and indicated by the yellow arrows. In regions where no fat is expected, for example, the blood pool (green), the fat signal is reduced by approximately 50%. On the other hand, in regions where fat is expected (red arrows) the fat signal increases locally up to 90%. B, Line plot showing the fat signal from FW^{NCB}_{NRR} (red), FW^{CB}_{NRR} (turquoise), and FW^{CB}_{MC} with $\Delta B_{0,NRR}$ (purple) and $\Delta B_{0,MC}$ maps (orange), the position is indicated by the dotted line in FW^{NCB}_{NRR}. MC led to a reduction of FWHM of 11% (purple) and 27% (orange) compared with NRR and CB fat image, indicated by the black arrows

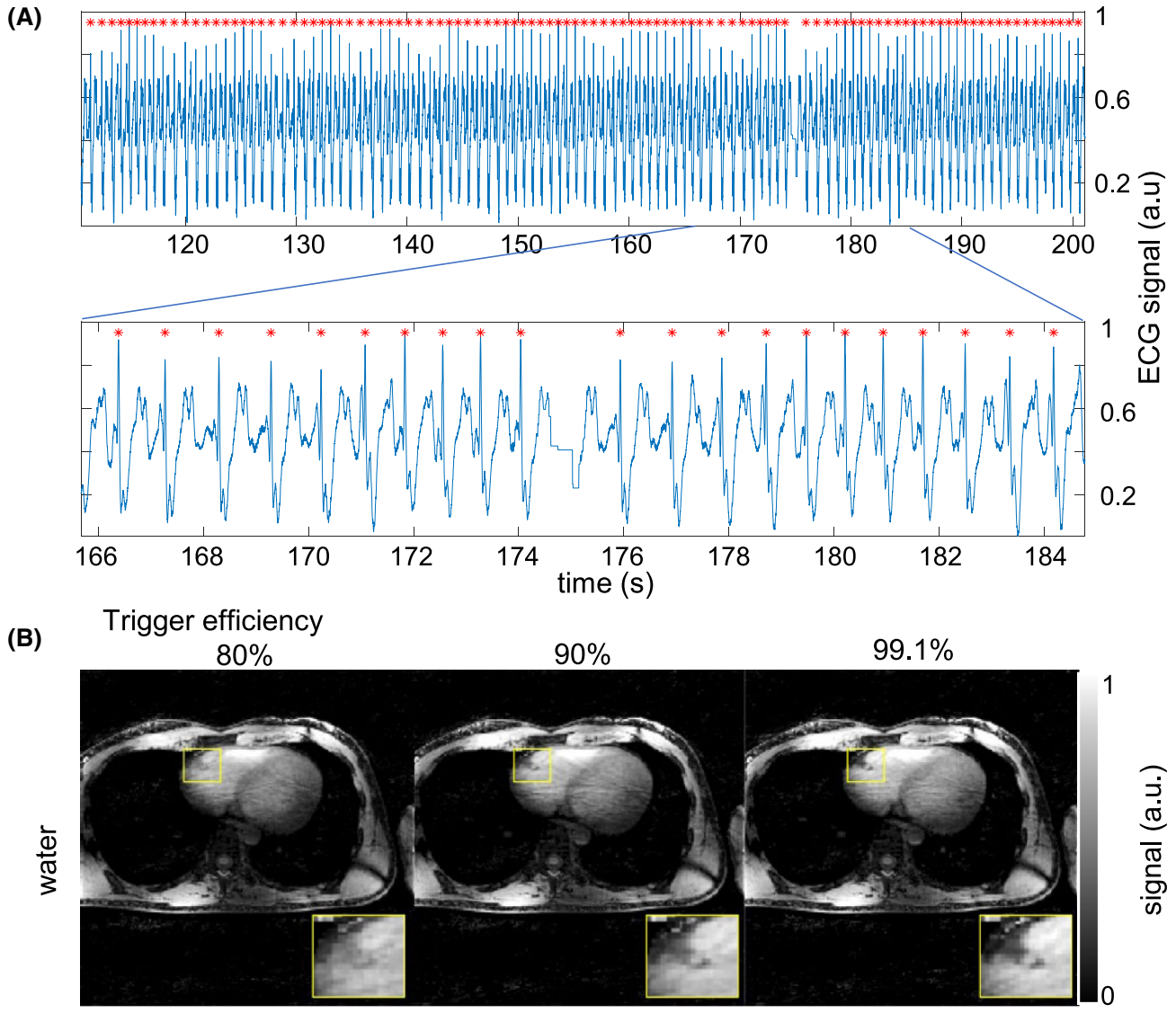

FIGURE 7 A, Illustration of the 90 s and 25 s of the entire ECG signal curve. As can be seen, the R-peak is detected by the scanner in all but one RR-interval, where the ECG signal appears to be corrupted for a short period of approximately half an RR-interval. For the entire acquisition, 4 of 438 were not correctly depicted in volunteer V9, resulting in 99.1% trigger efficiency. B, Transversal images showing 80%, 90%, and 99.1% trigger efficiency and the impact of the resulting fat and water images in diastole. Qualitatively, the edges and detailed structures such as the coronary artery become increasingly blurry with decreasing number of correct trigger points

was only 80%, since every third to sixth R-peak in the ECG curve appeared to be missing (Supporting Information Figure S4). To investigate the impact on the images, subfigure (B) shows resulting images after retrospectively removing every 5th and 10th trigger point, resulting in a trigger efficiency of 80%, 90%, and 99.1% for V7. The resulting images in Figure 7B, are qualitatively similar; however, the edges and small details become blurrier with decreasing number of correct trigger points.

Figure 8 shows reformatted images for V2 and V5 (BMI: 34.0 kg/m^2) shown in Supporting Information Figure S3, in short axis (SAX), long axis (LAX), and four-chamber view (4CV). A coronary artery can be seen in the water image of FW^{CB}_{MC} and in the corresponding FF images, denoted by the red arrow. FF for subcutaneous fat is calculated to 93 ± 3%. Figure 9 shows water images FW^{CB}_{MC} in diastole of V11 (BMI: 20.6 kg/m^2) with 1.4 mm^3 and 1.1 mm^3 isotropic resolution in two oblique views with depicted coronary arteries (blue and yellow box), which are surrounded by fat, showing no residual problems related to FA heterogeneity or residual motion. Note that, for the 1.1 mm^3 scan, not only has the resolution been increased by 27%, but also the reduction factor R has been increased by 26% compared to the 1.4 mm^3 scan.

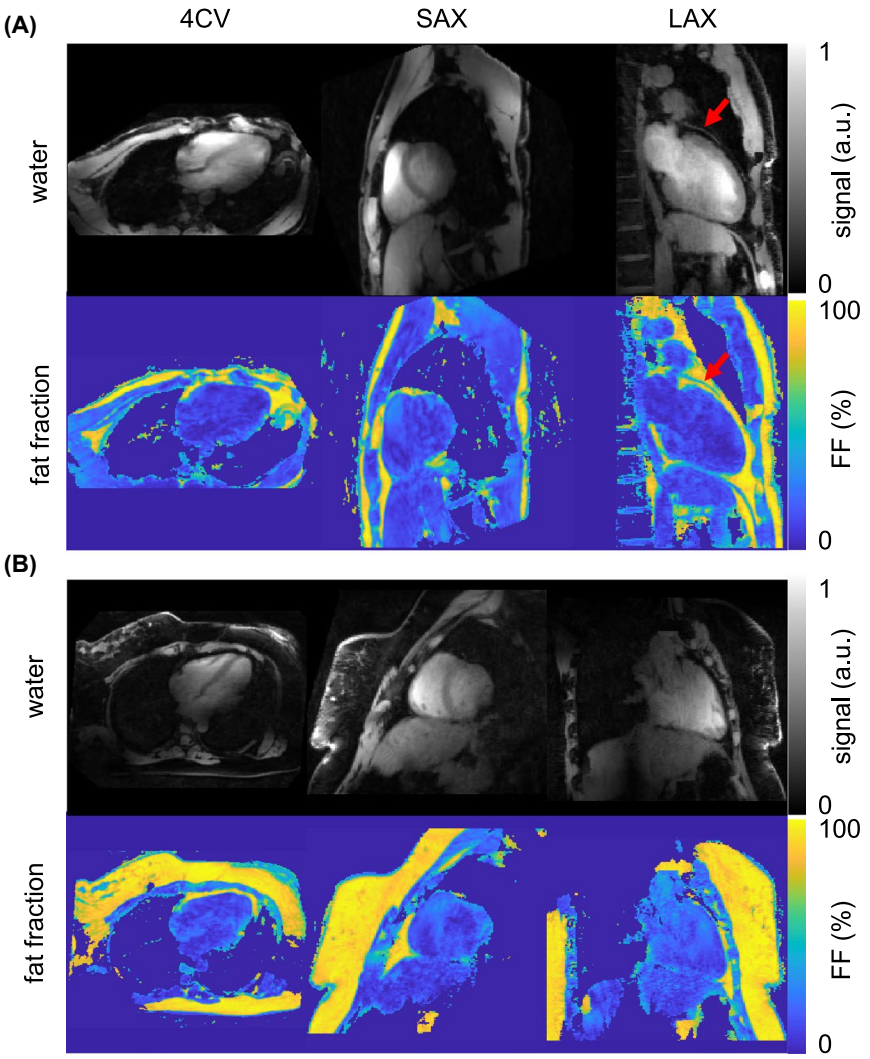

FIGURE 8 Resliced 3D volume of volunteer V2 and V5 showing 4CV, SAX, and LAX view showing water and FF images. The red arrows indicate a coronary artery in the water image, which is surrounded by fat as shown in the FF image. FF for subcutaneous fat is calculated to 93 ± 3%

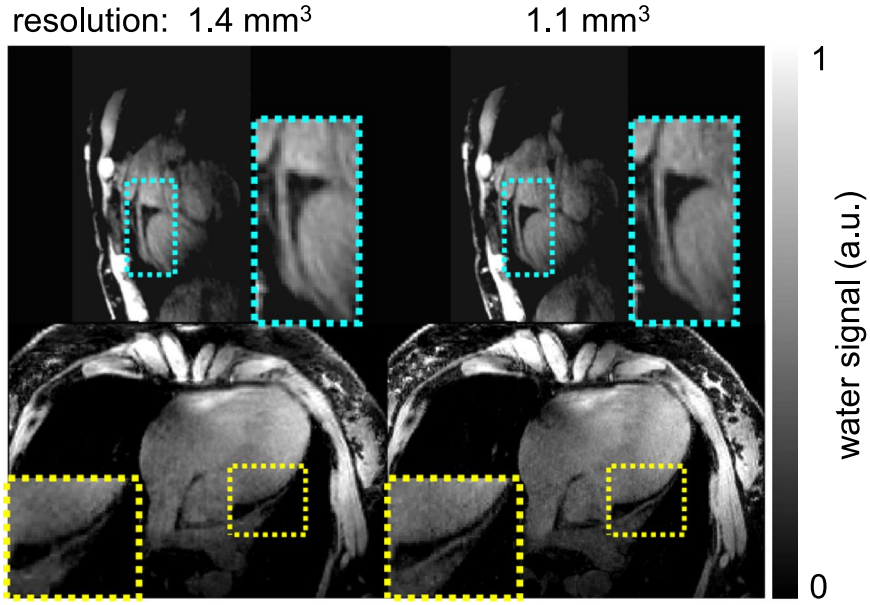

FIGURE 9 Resliced 3D volume FW^{NCR}_{NRR} of volunteer V11 showing double oblique view water images in diastole; boxes depict coronary arteries that are surrounded by fat

4 | DISCUSSION

This work demonstrates for the first time successful 3D cardiac FW imaging at UHF for a wide range of BMI and body shapes allowing cardiac phase-resolved fat and water images in arbitrary orientations. In addition to FW imaging, this work investigated the impact of shallow respiration and MC on the ΔB_0 distribution in the heart. Related to the FW frequency shifts only small deviations are caused by MC in the resulting $\Delta B_{0,MC}$ maps compared with the reference end-exhale $\Delta B_{0,RR}$ map. CB MC FW reconstruction reduced respiratory motion-induced blurring in the FW images and avoided flow artifacts in the end-diastolic FW images.

The 3D cardiac FW imaging at 7T requires proper B_1^+ management to avoid signal cancellations within the relatively large target region. Applications targeting the human body at 7T using either fixed volunteer-unspecific B_1^+ shimming,[21,23] tailored B_1^+ shimming,[58] or dynamic pTx techniques.[24,30] Fixed volunteer-unspecific approaches do not require additional RF management, but may lead to large B_1^+ variations within the target region[23] or can lead to an extended acquisition time if the TIAMO method is used.[32] In this work, tailored B_1^+ shimming was performed for three transversal slices covering the heart using channel-wise relative 3D B_1^+ maps obtained within the entire thorax. This approach was necessary because the default B_1^+ shim resulted in signal voids in the heart in nine volunteers. Although to our experience the size of the heart is at the limit of what can be homogenized with B_1^+ shimming on an eight-Tx channel system, the phase-only shimming approach yielded B_1^+ distributions without signal voids in all but one volunteer. For the one volunteer, magnitude and phase shimming was used to obtain a B_1^+ distribution without signal voids. This is reflected by the mean CV of the B_1^+ maps across all volunteers in the human heart with an unacceptable CV of 42% for the default shim, which was reduced to a CV of 24% with B_1^+ shimming. More homogeneous FA patterns may be obtained using dynamic pTx, such as kT point pulses as shown recently[24] ; however, here the different frequencies need to be considered during RF pulse design.[59] Nevertheless, the residual FA variations seem not to affect the proposed FW approach that is relying on magnitude and phase information. Within the 3D volume, sufficient signal was available in all volunteers to successfully demonstrate the feasibility of cardiac FW imaging at 7T.

The 3D triple-echo GRE-RPE sequence allows the acquisition of high-resolution images under free-breathing and, therefore, is highly beneficial for UHFs. This RPE trajectory in combination with MC has been previously applied in a patient study to improve the image quality of cardiac PET\MR images for localization of coronary plaques[38] and in healthy volunteers for more accurate peak flow determination[42] at 3T. In contrast to the applied self-navigation approach, which has proven valuable for estimating respiratory motion not only at lower fields, there are several approaches to track respiratory motion, including image-based navigators.[60] The latter is more difficult to acquire at UHF because the used B_1^+ shim setting has a strong influence on navigator performance, which can lead to unpredictable scan times and scan aborts. The estimated motion information from self-navigation did not suffer from local B_1^+ changes, and accurate motion minimization was ensured.

In order to keep the scan time short, MC is applied to use 100% of the acquired GRE-RPE data and to reduce the blurring caused by respiration and, thus, increase image resolution. In contrast to the retrospective respiratory-gated acquisition, the entire data set is available for cardiac binning, which reduces undersampling in the resulting cardiac bins. MC remaps each tissue voxel obtained at different respiratory motion phases into a single reference phase using motion vector fields. Thus, if ΔB_0 were to change over the respiratory cycle, a respiration-dependent signal phase term would be included in the resulting images that could affect the applied FW image reconstruction. Specifically, this may result in crosstalk between water and fat peaks, leading to swaps or incorrect FW values, as has been shown previously.[16] To investigate the extend of ΔB_0 across the respiratory cycle, 3D ΔB_0 maps have been acquired as a function of the respiratory phase, and changes in ΔB_0 have been investigated. While fairly strong spatial peak-to-peak ΔB_0 variations of 460 ± 50 Hz have been found across the heart, which match with values reported by other groups for a global shim,[61] the results demonstrate only limited ΔB_0 variations of -90 Hz at maximum and 35 Hz on average between expiration and inspiration for shallow-breathing, which confirm previous observations made for 2D transversal cardiac slices obtained at different respiratory phases.[48] Resulting MC ΔB_0 maps that incorporate signals from all respiratory phases and map them to the exhale phase show even fewer differences of 10 Hz on average to the exhale ΔB_0 map and such values can be regarded as small compared with the chemical shift between water and fat. It was found that the shape of the ΔB_0 distribution barely changes while its center frequency shifts as a function of respiration. This may be linked to the predominately translational motion of the heart in the HF direction, but further investigations are needed to fully characterize ΔB_0 changes across the respiratory cycle. Thus, for the present case of shallow-breathing, we show that it is sufficient to use NRR maps instead of the RR and MC ΔB_0 maps for further reconstruction. In addition, it is also possible to use ΔB_0 maps in the reference motion phase for MC, CB, FW separation,

but volunteer-specific parameter adjustment is required to estimate artifact-free ΔB_0 maps in the entire FOV, which was not necessary for MC or NRR ΔB_0 map estimation.

This study also has limitations. First, the tissue's relaxation times T_1 and T_2^* impact the FW quantification. In this work, a T_1 bias, that is, overestimation of FF,[6] is expected to remain by applying a TR of 6.1 ms and an actual FA of approximately 5° that is close to the expected Ernst angle. Thus, further corrections may be necessary.[62] Additionally, a T_2^* bias, that is, underestimation of the fat content,[6] was observed in the phantom evaluation of test tubes with different FW ratios (100%, 53%, and 26%, cf., Supporting Information Figure S5). A total of 8–9% lower fat content was measured for 100% and 26% FW ratio, and 21% lower fat content for 53% FW ratio. This bias could be reduced by T_2^* estimation, which has been realized in studies of fat quantification in the liver or other body parts with an increased number of echoes at lower field strength.[20,63] However, such deviations found in the 7T phantom data may not reflect the in vivo behavior because the relaxation times (fat: T_1 = 225 ms; T_2^* = 90 ms and water/agarose T_1 = 150 ms; T_2^* = 30 ms) differ from in vivo values. To quantify the FF and estimate its accuracy in vivo, further studies are needed to (1) compensate for the confounding factors and (2) validate the measurements with spectroscopy data, as has been done at lower fields.[64,65] Second, limitations arise with the 7T system in terms of the increased complexity of the overall measurement process. A contributing factor is the tailored calibration of the B_1^+ field, which is necessary to avoid complete signal cancellation. Despite a tight reconstruction and shimming procedure, an additional calibration time of about 10 minutes is required. Third, despite careful placement,[37] acquisition of an acceptable ECG signal is error-prone and remains difficult compared with lower field strength. Despite other findings,[66] a reliable ECG signal was obtained in 10 of 11 volunteers in this study as in Ref. [67]. We speculate that the poor efficiency found in one volunteer may be related to the respiratory motion, but a separate analysis is necessary. Fourth, the contrast between blood and myocardium is not very pronounced in T_1-weighted GRE sequences at UHF because of the similar T_1 values of blood and myocardium. At lower field strengths, T_2 preparation pulses are used to increase contrast. At UHF, the use of T_2 preparation pulses is challenging, and tailored approaches like VERSE pulses need to be used.[68] Fifth, the present work does not yet apply a resolution higher than currently used at clinical field strength, which is about (1.05–1.5 mm)^3 [17,45,69] isotropic. Increasing the resolution would require a detailed study of the echo spacing, which is currently 1.28 ms, thus pushing the current gradient system to its limits and requiring an increase in the echo spacing to non-noise-optimal spacings.[70] The aim of this work was rather to investigate the feasibility of the technique and to identify potential challenges that are associated with the high field in combination with the present techniques.

5 | CONCLUSIONS

Despite the known challenges in UHF body MRI posed by B_1^+ heterogeneity, spatial and temporal B_0 variations, and respiratory and cardiac motion, this work demonstrates the feasibility of 3D FW imaging at UHF for the whole heart. Based on this work, we intend to take advantage of UHF, such as higher SNR, by further developing the method to achieve improved spatial resolution with the aim to separate epicardial fat from small fat infiltrations in the right ventricle in the future. In addition, the workflow applied in this work can be used in other applications and push the field of UHF body MRI forward.

ACKNOWLEDGMENT

We thank Dr. Edyta Blaszczyk at Charité-Universitätsmedizin (Berlin, Germany) for the valuable discussions, and the authors gratefully acknowledge co-funding from the German Research Foundation (SCHM 2677/2-1 and GRK2260, BIOQIC).

ORCID

Sebastian Dietrich https://orcid.org/0000-0002-1610-909X
Christoph Stefan Aigner https://orcid.org/0000-0003-3618-9610
Johannes Mayer https://orcid.org/0000-0002-2500-445X
Christoph Kolbitsch https://orcid.org/0000-0002-4355-8368
Jeanette Schulz-Menger https://orcid.org/0000-0003-3100-1092
Tobias Schaeffter https://orcid.org/0000-0003-1310-2631
Sebastian Schmitter https://orcid.org/0000-0003-4410-6790

REFERENCES

1. Kellman P, Hernando D, Arai AE. Myocardial fat imaging. *Curr Cardiovasc Imaging Rep*. 2010;3:83-91.
2. Mertens LL, Friedberg MK. Imaging the right ventricle-current state of the art. *Nat Rev Cardiol*. 2010;7:551-563.
3. Jain A, Tandri H, Calkis H, Bluemke DA. Role of cardiovascular magnetic resonance imaging in arrhythmogenic right ventricular dysplasia. *J Cardiovasc Magn Reson*. 2008;10:1-14.
4. Calkins H. Arrhythmogenic right ventricular dysplasia/cardiomyopathy – three decades of progress. *Circ J*. 2015;79:901-913.
5. Bray TJP, Chouhan MD, Punwani S, Bainbridge A, Hall-Craggs MA. Fat fraction mapping using magnetic resonance imaging:

insight into pathophysiology. *The British Journal of Radiology*. 2017:20170344. http://dx.doi.org/10.1259/bjr.20170344
6. Kühn J-P, Hernando D, Mensel B, et al. Quantitative chemical shift-encoded MRI is an accurate method to quantify hepatic steatosis. *J Magn Reson Imaging*. 2014;39:1494-1501.
7. Eggers H, Börnert P. Chemical shift encoding-based water-fat separation methods. *J Magn Reson Imaging*. 2014;40:251-268.
8. Reeder SB, McKenzie CA, Pineda AR, et al. Water-fat separation with IDEAL gradient-echo imaging. *J Magn Reson Imaging*. 2007;25:644-652.
9. Bley TA, Wieben O, François CJ, Brittain JH, Reeder SB. Fat and water magnetic resonance imaging. *J Magn Reson Imaging*. 2010;31:4-18.
10. Berglund J, Johansson L, Ahlström H, Kullberg J. Three-point Dixon method enables whole-body water and fat imaging of obese subjects. *Magn Reson Med*. 2010;63:1659-1668.
11. Hamilton G, Yokoo T, Bydder M. In vivocharacterization of the liver fat1H MR spectrum. *NMR in Biomedicine*. 2011;24:784-790. http://dx.doi.org/10.1002/nbm.1622
12. Reeder SB, Pineda AR, Wen Z, et al. Iterative decomposition of water and fat with echo asymmetry and least-squares estimation (IDEAL) fat spin-echo imaging of the ankle: Initial clinical experience. *Magn Reson Med*. 2005;54:636-644.
13. Peterson P, Trinh L, Månsson S. Quantitative 1H MRI and MRS of fatty acid composition. *Magn Reson Med*. 2021;85:49-67.
14. Leporq B, Lambert SA, Ronot M, Vilgrain V, Van Beers BE. Quantification of the triglyceride fatty acid composition with 3.0 T MRI. *NMR Biomed*. 2014;27:1211-1221.
15. Benkert T, Feng L, Sodickson DK, Chandarana H, Block KT. Free-breathing volumetric fat/water separation by combining radial sampling, compressed sensing, and parallel imaging. *Magn Reson Med*. 2017;78:565-576.
16. Tan Z, Voit D, Kollmeier JM, Uecker M, Frahm J. Dynamic water/fat separation and B0 inhomogeneity mapping—joint estimation using undersampled triple-echo multi-spoke radial FLASH. *Magn Reson Med*. 2019;82:1000-1011.
17. Munoz C, Bustin A, Neji R, et al. Motion-corrected 3D whole-heart water-fat high-resolution late gadolinium enhancement cardiovascular magnetic resonance imaging. *J Cardiovasc Magn Reson*. 2020;22:1-13.
18. Kolbitsch C, Mayer J, Cipriani A, Blaszczyk E, Schulz-menger J. Motion-corrected 3D high-resolution fat-water imaging of the heart. Proc 27th Annu Meet ISMRM. 2019;0402.
19. Berglund J, Ahlström H, Kullberg J. Model-based mapping of fat unsaturation and chain length by chemical shift imaging-phantom validation and in vivo feasibility. *Magn Reson Med*. 2012;68:1815-1827.
20. Schneider M, Benkert T, Solomon E, et al. Free-breathing fat and R2* quantification in the liver using a stack-of-stars multi-echo acquisition with respiratory-resolved model-based reconstruction. *Magn Reson Med*. 2020;84:2592-2605.
21. Philips BWJ, Fortuin AS, Orzada S, Scheenen TWJ, Maas MC. High resolution MR imaging of pelvic lymph nodes at 7 Tesla. *Magn Reson Med*. 2017;78:1020-1028.
22. Erturk MA, Li X, Van De Moortele PF, Ugurbil K, Metzger GJ. Evolution of UHF body imaging in the human torso at 7T: technology, applications, and future directions. *Top Magn Reson Imaging*. 2019;28:101-124.
23. van der Velden TA, Schmitz AM, Gilhuijs KGA, et al. Fat suppression techniques for obtaining high resolution dynamic contrast enhanced bilateral breast MR images at 7 T. *Magn Reson Imaging*. 2016;34:462-468.
24. Aigner CS, Dietrich S, Schmitter S. Three-dimensional static and dynamic parallel transmission of the human heart at 7 T. *NMR Biomed*. 2021;34:1-15.
25. Schmitter S, Schnell S, Uğurbil K, Markl M, Van de Moortele PF. Towards high-resolution 4D flow MRI in the human aorta using kt-GRAPPA and B1+ shimming at 7T. *J Magn Reson Imaging*. 2016;44:486-499.
26. Hess AT, Bissell MM, Ntusi NABB, et al. Aortic 4D flow: quantification of signal-to-noise ratio as a function of field strength and contrast enhancement for 1.5T, 3T, and 7T. *Magn Reson Med*. 2015;73:1864-1871.
27. Metzger GJ, Snyder C, Akgun C, Vaughan T, Ugurbil K, Van De Moortele PF. Local B1+ shimming for prostate imaging with transceiver arrays at 7T based on subject-dependent transmit phase measurements. *Magn Reson Med*. 2008;59:396-409.
28. Snyder CJ, DelaBarre L, Metzger GJ, et al. Initial results of cardiac imaging at 7 Tesla. *Magn Reson Med*. 2009;61:517-524.
29. Wu X, Schmitter S, Auerbach EJ, Uğurbil K, Van de Moortele P-F. Mitigating transmit B1 inhomogeneity in the liver at 7T using multi-spoke parallel transmit RF pulse design. *Quant Imaging Med Surg*. 2014;4:4-10.
30. Schmitter S, DelaBarre L, Wu X, et al. Cardiac imaging at 7 Tesla: single- and two-spoke radiofrequency pulse design with 16-channel parallel excitation. *Magn Reson Med*. 2013;70:1210-1219.
31. Aigner CS, Dietrich S, Schaeffter T, Schmitter S. Calibration-free pTx of the human heart at 7T via 3D universal pulses. Proc. 29th Annu. Meet. ISMRM. 2021;777.
32. Orzada S, Maderwald S, Poser BA, Bitz AK, Quick HH, Ladd ME. RF excitation using time interleaved acquisition of modes (TIAMO) to address B1 inhomogeneity in high-field MRI. *Magn Reson Med*. 2010;64:327-333.
33. McClelland JR, Hawkes DJ, Schaeffter T, King AP. Respiratory motion models: a review. *Med Image Anal*. 2013;17:19-42.
34. Earls JP, Ho VB, Foo TK, Castillo E, Flamm SD. Cardiac MRI: recent progress and continued challenges. *J Magn Reson Imaging*. 2002;16:111-127.
35. Taviani V, Hernando D, Francois CJ, et al. Whole-heart chemical shift encoded water-fat MRI. *Magn Reson Med*. 2014;72:718-725.
36. Henningsson M, Brundin M, Scheffel T, Edin C, Viola F, Carlhäll CJ. Quantification of epicardial fat using 3D cine Dixon MRI. *BMC Med Imaging*. 2020;20:1-9.
37. Suttie JJ, Delabarre L, Pitcher A, et al. 7 Tesla (T) human cardiovascular magnetic resonance imaging using FLASH and SSFP to assess cardiac function: validation against 1.5T and 3T. *NMR Biomed*. 2012;25:27-34.
38. Mayer J, Wurster T-H, Schaeffter T. Imaging coronary plaques using 3D motion-compensated [18F]NaF PET/MR. *European Journal of Nuclear Medicine and Molecular Imaging*. 2021;48:2455-2465.
39. Buerger C, Clough RE, King AP, Schaeffter T, Prieto C. Nonrigid motion modeling of the liver from 3-D undersampled self-gated golden-radial phase encoded MRI. *IEEE Trans Med Imaging*. 2012;31:805-815.
40. Feng LI, Coppo S, Piccini D, et al. 5D whole-heart sparse MRI. *Magn Reson Med*. 2018;79:826-838.
41. Dietrich S, Aigner CS, Kolbitsch C, et al. 3D Free-breathing multichannel absolute B1+ Mapping in the human body at 7T. *Magn Reson Med*. 2021;85:2552-2567.

42. Kolbitsch C, Bastkowski R, Schäffter T, et al. Respiratory motion corrected 4D flow using golden radial phase encoding. *Magn Reson Med*. 2020;83:635-644.
43. Coppo S, Piccini D, Bonanno G, et al. Free-running 4D whole-heart self-navigated golden angle MRI: initial results. *Magn Reson Med*. 2015;74:1306-1316.
44. Küstner T, Bustin A, Jaubert O, et al. Fully self-gated free-running 3D Cartesian cardiac CINE with isotropic whole-heart coverage in less than 2 minutes. *NMR Biomed*. 2021;34:1-13.
45. Pang J, Sharif B, Fan Z, et al. ECG and navigator-free four-dimensional whole-heart coronary MRA for simultaneous visualization of cardiac anatomy and function. *Magn Reson Med*. 2014;72:1208-1217.
46. Hock M, Terekhov M, Stefanescu MR, et al. B0 shimming of the human heart at 7T. *Magn Reson Med*. 2021;85:182-196.
47. Reeder SB, Faranesh AZ, Boxerman JL, McVeigh ER. In vivo measurement of T2(*) and field inhomogeneity maps in the human heart at 1.5 T. *Magn Reson Med*. 1998;39:988-998.
48. Schmitter S, Wu X, Uğurbil K, Van De Moortele PF. Design of parallel transmission radiofrequency pulses robust against respiration in cardiac MRI at 7 Tesla. *Magn Reson Med*. 2015;74:1291-1305.
49. Rueckert D, Sonoda LI, Hayes C, Hill DLG, Leach MO, Hawkes DJ. Nonrigid registration using free-form deformations: application to breast MR images. *IEEE Trans Med Imaging*. 1999;18:712-721.
50. Pruessmann KP, Weiger M, Peter B, Boesiger P. Advances in sensitivity encoding with arbitrary k-space trajectories. *Magn Reson Med*. 2001;46:638-651.
51. Lustig M, Donoho DL, Santos JM, Pauly JM. Compressed sensing MRI. *IEEE Signal Process Mag*. 2008;25:72-82.
52. Batchelor PG, Atkinson D, Irarrazaval P, Hill DLG, Hajnal J, Larkman D. Matrix description of general motion correction applied to multishot images. *Magn Reson Med*. 2005;54:1273-1280.
53. Yarnykh VL. Actual flip-angle imaging in the pulsed steady state: a method for rapid three-dimensional mapping of the transmitted radiofrequency field. *Magn Reson Med*. 2007;57:192-200.
54. Yu H, Shimakawa A, McKenzie CA, et al. Phase and amplitude correction for multi-echo water-fat separation with bipolar acquisitions. *J Magn Reson Imaging*. 2010;31:1264-1271.
55. Smith DS, Berglund J, Kullberg J, Ahlström H, Avison MJ, Welch EB. Optimization of fat-water separation algorithm selection and options using image-based metrics with validation by ISMRM fat-water challenge datasets. Proc. 21st Annu. Meet. ISMRM, Salt Lake City, Utah: 2013, p. 2413.
56. Walsh DO, Gmitro AF, Marcellin MW. Adaptive reconstruction of phased array MR imagery. *Magn Reson Med*. 2000;43:682-690.
57. Reeder SB, Sirlin CB. Quantification of liver fat with magnetic resonance imaging. *Magn Reson Imaging Clin N Am*. 2010;18:337-357.
58. Laader A, Beiderwellen K, Kraff O, et al. 1.5 versus 3 versus 7 Tesla in abdominal MRI: a comparative study. *PLoS One*. 2017;12:1-18.
59. Setsompop K, Alagappan V, Gagoski BA, et al. Broadband slab selection with B1+ mitigation at 7T via parallel spectral-spatial excitation. *Magn Reson Med*. 2009;61:493-500.
60. van Heeswijk RB, Bonanno G, Coppo S, Coristine A, Kober T, Stuber M. Motion compensation strategies in magnetic resonance imaging. *Crit Rev Biomed Eng*. 2012;40:99-119.
61. Hezel F, Thalhammer C, Waiczies S, Schulz-Menger J, Niendorf T. High spatial resolution and temporally resolved T2* mapping of normal human myocardium at 7.0 Tesla: an ultrahigh field magnetic resonance feasibility study. *PLoS One*. 2012;7:1-14.
62. Kühn J-P, Jahn C, Hernando D, et al. T1 bias in chemical shift-encoded liver fat-fraction: role of the flip angle. *J Magn Reson Imaging*. 2014;40:875-883.
63. Yu H, Shimakawa A, McKenzie CA, Brodsky E, Brittain JH, Reeder SB. Multiecho water-fat separation and simultaneous R*2 estimation with multifrequency fat spectrum modeling. *Magn Reson Med*. 2008;60:1122-1134.
64. Grimm A, Meyer H, Nickel MD, et al. A comparison between 6-point Dixon MRI and MR spectroscopy to quantify muscle fat in the thigh of subjects with sarcopenia. *J Frailty Aging*. 2019;8:21-26.
65. Grimm A, Meyer H, Nickel MD, et al. Evaluation of 2-point, 3-point, and 6-point Dixon magnetic resonance imaging with flexible echo timing for muscle fat quantification. *Eur J Radiol*. 2018;103:57-64.
66. Krug JW, Rose G, Clifford GD, Oster J. ECG-based gating in ultra high field cardiovascular magnetic resonance using an independent component analysis approach. *J Cardiovasc Magn Reson*. 2013;15:1-13.
67. Stäb D, Roessler J, O'Brien K, Hamilton-Craig C, Barth M. ECG triggering in ultra-high field cardiovascular MRI. *Tomography*. 2016;2:167-174.
68. Conolly S, Nishimura D, Macovski A, Glover G. Variable-rate selective excitation. *J Magn Reson*. 1988;78:440-458.
69. Kolbitsch C, Prieto C, Buerger C, et al. Prospective high-resolution respiratory-resolved whole-heart MRI for image-guided cardiovascular interventions. *Magn Reson Med*. 2012;68:205-213.
70. Pineda AR, Reeder SB, Wen Z, Pelc NJ. Cramér-Rao bounds for three-point decomposition of water and fat. *Magn Reson Med*. 2005;54:625-635.

SUPPORTING INFORMATION

Additional supporting information may be found in the online version of the article at the publisher's website.

FIGURE S1 Shows Figure 3 with unfiltered RR ΔB_0 maps
FIGURE S2 ROI_{heart} for exhale motion phase as an overlay on GRE image for three orthogonal views of all eleven volunteers
FIGURE S3 B_1^+ shimmed, motion-compensated, and cardiac binned fat-water images in the end-diastolic phase are shown for all eleven volunteers in 3 orthogonal views with BMI ranging from 19 to 34 kg/m^2. As can be clearly seen, the fat and water content could be robustly separated across different body geometries around the heart. Furthermore, signal voids caused by destructive B_1^+ interference in the heart could be avoided in all volunteers. Note that images were not corrected by receive profiles (B_1^-)
FIGURE S4 ECG curve of volunteer V6 with 80% trigger efficiency. (A) First 90 and 20 seconds and (B) interval from 330 to 420 seconds with zoom between 338 and 355 seconds with corresponding trigger points (red asterisk)

FIGURE S5 The FW phantom consists of a bowl filled with agarose containing three oil/agarose mixture tubes. To validate the fat-water separation and quantification the bowl-shape phantom (max. diameter = 20 cm, height = 10.0 cm) was used, filled with water, 2% agaroses, 0,2% sodium chloride, 0.1% copper sulfate (which corresponds to $\sigma_{\text{phantom}} = 0.4\,\text{s/m}, \varepsilon_r = 80$) containing 3 tubes (diameter = 2 cm, height = 8 cm) with different mass fractions of olive oil to water-agarose emulsion (26%/53%/100%). Subfigure (A) shows triple-echo GRE-RPE magnitude data, reconstructed water, fat and fat-fraction images of a coronal slice. Qualitatively fat and water content were separated. Subfigure (B) shows corresponding filtered line plots taken from positions indicated in the fat-fraction image with calculated mean FF of 17 ± 6%, 32 ± 5%, 92 ± 6% for tube content of 26%,53%, and 100% fat mass

VIDEO S1 Resliced 3D volume of volunteer V2 showing four-chamber (4CH), short axis (SAX), and long axis (LAX) view with water and fat fraction (FF) information in 5 cardiac phases

How to cite this article: Dietrich S, Aigner CS, Mayer J, et al. Motion-compensated fat-water imaging for 3D cardiac MRI at ultra-high fields. *Magn Reson Med*. 2022;87:2621–2636. doi:10.1002/mrm.29144